



**AFRL-OSR-VA-TR-2015-0179**

---

**ENERGY HARVESTING A NANO-SCALE BASED MAGNETO-  
THERMAL-ELECTRIC ELEMENT**

**Greg Carman  
UNIVERSITY OF CALIFORNIA LOS ANGELES**

---

**05/21/2015  
Final Report**

**DISTRIBUTION A: Distribution approved for public release.**

Air Force Research Laboratory  
AF Office Of Scientific Research (AFOSR)/RTD  
Arlington, Virginia 22203  
Air Force Materiel Command

<b>REPORT DOCUMENTATION PAGE</b>				Form Approved OMB No. 0704-0188	
<p>The public reporting burden for this collection of information is estimated to average 1 hour per response, including the time for reviewing instructions, searching existing data sources, gathering and maintaining the data needed, and completing and reviewing the collection of information. Send comments regarding this burden estimate or any other aspect of this collection of information, including suggestions for reducing the burden, to Department of Defense, Executive Services, Directorate (0704-0188). Respondents should be aware that notwithstanding any other provision of law, no person shall be subject to any penalty for failing to comply with a collection of information if it does not display a currently valid OMB control number.</p> <p>PLEASE DO NOT RETURN YOUR FORM TO THE ABOVE ORGANIZATION.</p>					
<b>1. REPORT DATE (DD-MM-YYYY)</b> 17-07-2015		<b>2. REPORT TYPE</b> Final Performance		<b>3. DATES COVERED (From - To)</b> 01-09-2009 to 28-02-2015	
<b>4. TITLE AND SUBTITLE</b> ENERGY HARVESTING A NANO-SCALE BASED MAGNETO-THERMAL-ELECTRIC ELEMENT				<b>5a. CONTRACT NUMBER</b>	
				<b>5b. GRANT NUMBER</b> FA9550-09-1-0620	
				<b>5c. PROGRAM ELEMENT NUMBER</b>	
<b>6. AUTHOR(S)</b> Greg Carman				<b>5d. PROJECT NUMBER</b>	
				<b>5e. TASK NUMBER</b>	
				<b>5f. WORK UNIT NUMBER</b>	
<b>7. PERFORMING ORGANIZATION NAME(S) AND ADDRESS(ES)</b> UNIVERSITY OF CALIFORNIA LOS ANGELES 11000 KINROSS AVE STE 102 LOS ANGELES, CA 90095-0001 US				<b>8. PERFORMING ORGANIZATION REPORT NUMBER</b>	
<b>9. SPONSORING/MONITORING AGENCY NAME(S) AND ADDRESS(ES)</b> AF Office of Scientific Research 875 N. Randolph St. Room 3112 Arlington, VA 22203				<b>10. SPONSOR/MONITOR'S ACRONYM(S)</b> AFOSR	
				<b>11. SPONSOR/MONITOR'S REPORT NUMBER(S)</b>	
<b>12. DISTRIBUTION/AVAILABILITY STATEMENT</b> A DISTRIBUTION UNLIMITED: PB Public Release					
<b>13. SUPPLEMENTARY NOTES</b>					
<b>14. ABSTRACT</b> <p>In this study we investigated/developed innovative thermomagnetic harvesting methods and materials that transduce waste heat into electrical energy. Initially we focused on gadolinium (Gd) single domain nanostructures which we predicted to have a thermomagnetic harvesting efficiency of approximately 30% of the Carnot limit. In this study, we discovered that more ordered transitions led to higher transduction efficiencies. Utilizing this phenomenon, we explored the effect of order-to-order spin reorientation harvesting in neodymium cobalt (NdCo5). Analytical modeling showed that NdCo5 could achieve an energy density greater than 2 MJ/m3 with an efficiency of approximately 22% of the Carnot limit. This report overviews the body of literature related to the thermomagnetic field, provides a detailed analysis of the UCLA modeling effort, and describes fabrication and testing techniques used to create and evaluate nano-structured thermomagnetic materials. This work should encourage others in the community to begin a closer evaluation of thermomagnetic energy harvesting methods.</p>					
<b>15. SUBJECT TERMS</b> Thermo-magnetic Energy Harvest, Thin-film Ferromagnetic Materials, Nanostructures					
<b>16. SECURITY CLASSIFICATION OF:</b>			<b>17. LIMITATION OF ABSTRACT</b>	<b>18. NUMBER OF PAGES</b>	<b>19a. NAME OF RESPONSIBLE PERSON</b> Greg Carman
<b>a. REPORT</b>  U	<b>b. ABSTRACT</b>  U	<b>c. THIS PAGE</b>  U			<b>19b. TELEPHONE NUMBER (Include area code)</b> 310-825-6030

Standard Form 298 (Rev. 8/98)  
Prescribed by ANSI Std. Z39.18

**ENERGY HARVESTING A NANO-SCALE BASED MAGNETOTHERMAL-ELECTRIC ELEMENT**

Grant Number FA9550-09-1-0620

Greg P. Carman, Kyle Wetzlar, Ray Hsu, and Sam Sandoval  
Mechanical & Aerospace Engineering Department, UCLA  
Los Angeles CA, 90024  
[carman@seas.ucla.edu](mailto:carman@seas.ucla.edu), 310-825-6030

***Abstract:***

In this study we evaluated the efficiencies of various thermomagnetic harvesting methods and materials. Initially we focused on producing gadolinium (Gd) single domain nanostructures which we predicted to have a thermomagnetic harvesting efficiency of approximately 30% of the Carnot limit. We successfully deposited epitaxial thin films of Gd which exhibited a spin-reorientation response and saw a reduction in Curie temperature when compared to bulk values. Unfortunately, we were unable to produce single domain elements using the lift off methods attempted. This was attributed to poor sidewall coating of the capping layer which led to a non-uniform Gd morphology and stacking faults that significantly reduced the saturation magnetic moment of the material. Upon examining the other single element magnetic materials in the literature, we discovered that more ordered transitions led to higher transduction efficiencies. Utilizing this phenomenon, we explored the effect of order-to-order spin reorientation harvesting in neodymium cobalt (NdCo<sub>5</sub>). Analytical modeling showed that NdCo<sub>5</sub> operating about its spin-reorientation temperature could achieve an energy density greater than 2 MJ/m<sup>3</sup> with an efficiency of approximately 22% of the Carnot limit. We attempted to produce epitaxial NdCo<sub>5</sub> by the same sputtering methodology used to fabricate the Gd films, but every combination of sputter and annealing parameters yielded highly textured yet non-aligned crystal morphologies. While we were unsuccessful in producing a working prototype, we garnered significant knowledge about the physics governing thermomagnetic transformations to pave the way for future work in this area. This report overviews the body of literature related to the thermomagnetic field, provides a detailed analysis of the UCLA modeling effort, and describes fabrication and testing techniques used to create and evaluate nano-structured thermomagnetic materials.

## 1.0 Background

All ferromagnetic materials experience a thermally induced second order phase transformation and transform from the ferromagnetic ordered state, where the magnetic moments prefer to align with one another yielding a spontaneous magnetization, to a disordered paramagnetic state, wherein the thermal energy experienced by each magnetic spin overcomes the aligning force and the material no longer appears magnetic to an outside observer. The temperature at which this transition occurs is known as the Curie Point ( $T_c$ ). By oscillating a magnetic material about this temperature, thermal energy can be transduced into magnetic energy, where it can be harvested as useable electrical energy utilizing the principles of electromagnetic generators.

The first attempt at thermomagnetic transduction was proposed by Nicola Tesla<sup>1</sup> in his 1889 patent, Thermo-magnetic Motor, wherein he showed how a thermally oscillated magnetic system could generate mechanical work. However, utilizing such a system to generate electrical power wasn't explored until Brillouin and Iskenderian<sup>2</sup> in 1948 . They proposed that a ferromagnetic material can perform magnetic work on a coil by flux oscillations which occur as the material is thermally cycled about its Curie Point ( $T_c$ ). Their model consisted of a prototypical Carnot cycle: heating and cooling the device in the presence of a varying magnetic field, wherein electrical energy is produced by the flux change in the magnetic material during the two adiabatic portions of the cycle. Their phenomenological analysis suggested that, in the limiting case, device efficiencies as high as 55% of the Carnot limit are possible.

One of the major obstacles in experimentally verifying this theory in the 1940's was the lack of ferromagnetic materials whose  $T_c$  was near room temperature. Therefore, this area remained dormant for the next decade. In 1959, Elliot et al<sup>3</sup> experimentally evaluated gadolinium (Gd) for use in a thermomagnetic energy harvesting system operating at room temperature. However, when actual power density calculations were made, Elliot's thermomagnetic generator failed to produce any significant power outputs. One of the main issues cited at this time was the lack of sufficiently strong magnets to bias the structures.

Following the development of rare earth magnets, in the 1980's Kirol et al<sup>4</sup> proposed a regenerative thermomagnetic cycle for increased power output. This regenerative thermomagnetic approach suggests a maximum relative efficiency ( $\eta_{rel}$ ) of 75 %. However, this approach was never experimentally attempted. In 1991, Solomon et al<sup>5-7</sup> designed and evaluated a thermomagnetic generator on the scale

of a large power plant (e.g. Hoover Dam) using Yttrium Iron ( $\text{Y}_2\text{Fe}_{17}$ ) as the ferromagnetic switch.  $\text{Y}_2\text{Fe}_{17}$  was chosen since its Curie temperature could be varied by compositional modifications. While advancing the field of regenerative thermomagnetic energy harvesting, the negligible power output limited the usefulness of this structure.

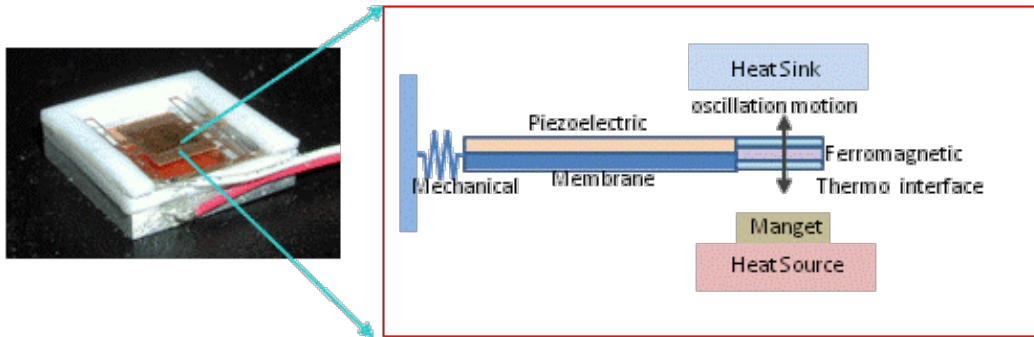


**Figure 1: Illustration of concept using layered thin film along with thermal and magnetic fields**

Following this body of literature, UCLA began conducting studies on macro and nanoscale thermomagnetic energy harvesting structures, postulating that significant improvements in efficiency and energy density could be made at reduced length scales. The method being used to harvest these magnetic changes and convert the energy into a usable electrical form is by harnessing a multiferroic composite of magnetic and piezoelectric material. This system, illustrated in Figure 1, consists of a layered beam element containing a ferromagnetic switch (e.g. Gd, which has a room-temperature phase transformation), a classic ferroelectric like lead zirconate titanate (PZT), a heat source containing a hard ferromagnetic material (e.g. neodymium iron boron ( $\text{NdFeB}$ )), and a heat sink. At the heat source, the  $\text{NdFeB}$  magnet produces a magnetic field that induces an attractive force in the Gd material, due to magnetostatics and domain wall motion. As the beam bends, the beam produces charge on the piezoelectric surface, which is harvested as electrical energy. When the Gd touches the hot source, it heats up and undergoes a second order transformation into a paramagnetic (i.e. non-magnetic) state, releasing the beam from the hot source. This returns the beam to the environmentally available cold sink and generates additional charge on the piezoelectric. Once in contact with the cold sink, it undergoes a reverse second order transformation back into a ferromagnetic state that is once again magnetically attracted to the environmentally available hot source. This cyclical process repeats itself and produces electrical energy output. UCLA has demonstrated the concept at the mesoscopic level (1 cm); however, the measured efficiencies of the current device are on the order of 10-20% of Carnot, i.e. similar to the Seebeck thermoelectric device.

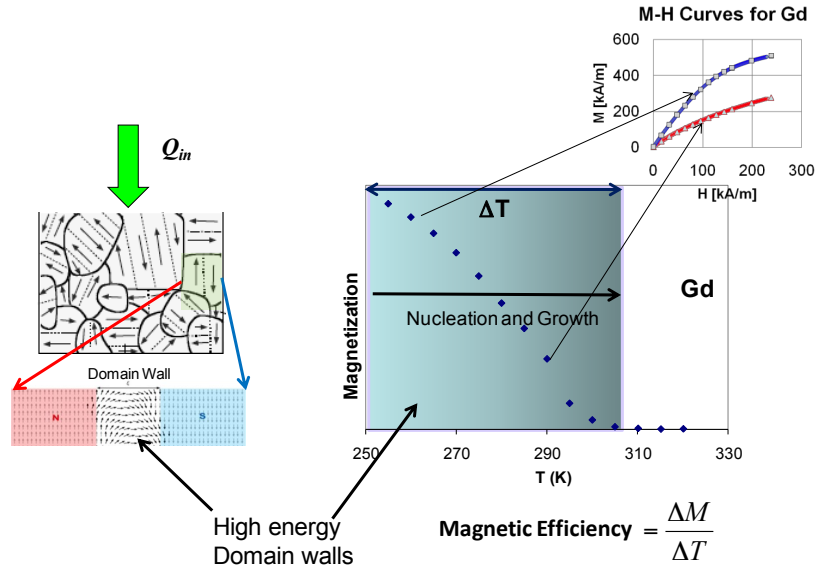


Figure 2: Illustration of domain walls and calculation of efficiency.

The UCLA device operation is represented by exchanging thermal energy for magnetic energy as illustrated in Figure 2. Heating the ferromagnetic material by  $\Delta T$  (i.e. through its Curie temperature) requires a specific amount of thermal energy as illustrated in Figure 2. This represents the input energy into the device. When the ferromagnetic material is cooled below its Curie temperature, the ferromagnetic material stores some of this input thermal energy as magnetization in the material. The remainder of the thermal energy is delivered to the cold source as waste heat and represents thermal energy loss. The magnetic energy stored in the ferromagnetic material represents the available energy to harvest as electricity.

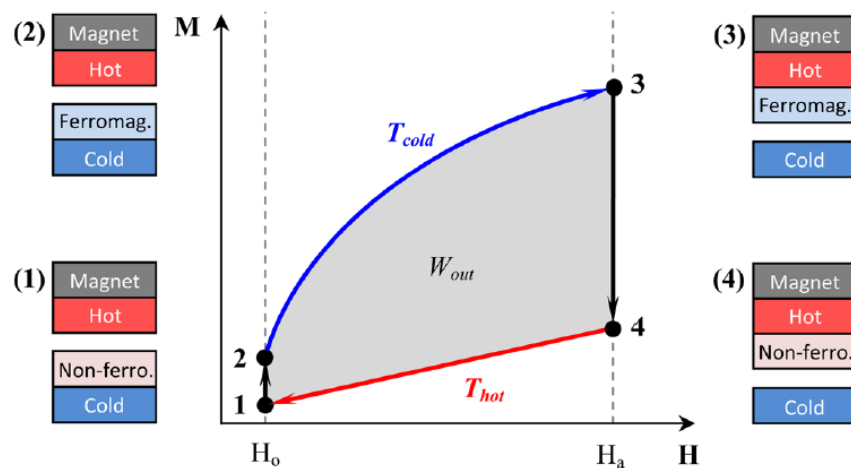


Figure 3: Isothermal magnetization curves and thermomagnetic cycle.

An idealized thermomagnetic cycle which utilizes UCLA's multiferroic device design is shown in Figure 3 along with a plot of magnetization as a function of magnetic field (M-H plot) for two different temperatures straddling the Curie Point. The four illustrations shown in Figure 1 contain a magnetic heat source which generates a magnetic field to attract the magnetic working element and a cold heat sink to shuttle packets of thermal energy to. The process can be described as follows: Initially, at point 1, the temperature of the material is above  $T_c$  (at  $T_{hot}$ ) and is therefore non-ferromagnetic. By bringing the material into thermal contact with a cold reservoir, the temperature drops to  $T_{cold}$  ( $T_{cold} < T_c$ ) and the material becomes ferromagnetic at point 2. During this process, the material is subjected to a magnetic field which increases the magnetization of the material to point 3 on the M-H plot. Simultaneously, the material is brought into thermal contact with the hot reservoir where the temperature again increases to  $T_{hot}$  at point 4 and the material becomes non-ferromagnetic, returning to the cold side at point 1 and thus completing the cycle.

In order to compute the amount of energy available per cycle we needed to consider the thermodynamics of the system. The thermomagnetic cycle involved has a net work which can be defined as the area between isothermal magnetization curves. If we consider the following work expression (expressed in cgs, where the units are erg/cm<sup>3</sup>)

$$W_{out} = -\frac{1}{4\pi} \oint_{cycle} HdB = -\frac{1}{4\pi} \oint_{cycle} (HdH + 4\pi HdM(T, H)) \quad (1.1)$$

Where B is the magnetic induction, H is the magnetic field, and M is the magnetization. Since the integral of the HdH term is zero over a complete cycle, Equation 1.1 reduces to

$$W_{out} = -\oint_{cycle} HdM(T, H). \quad (1.2)$$

By utilizing energy conservation, the heat that must be input into the system is defined as follows:

$$Q_{in} = Q_{out} + W_{out} = \rho \int_{T_{cold}}^{T_{hot}} C_p(T) dT + T \int dS_m + W_{out} \cong \rho \int_{T_{cold}}^{T_{hot}} C_p(T) dT \quad (1.3)$$

Where  $\rho$  is the density,  $C_p$  is the specific heat at constant pressure, and  $S_m$  is the magnetic entropy associated with irreversible domain wall motion and nucleation. For small H fields, the integral of the specific heat term is much larger than the other two terms relative to the magnetization of the material, and thus, the heat equation can be simplified as prescribed in equation 1.3. With the work out and heat in equations defined for the system, the absolute efficiency can be described as follows:

$$\eta_{abs} = \frac{|W_{out}|}{Q_{in}} = \frac{\oint_{cycle} HdM(T, H)}{T_{Hot} \rho \int_{T_{cold}} C_p(T) dT}. \quad (1.4)$$

The absolute efficiency can be compared to the limiting case of the Carnot efficiency ( $\eta_{carnot}$ ) operating between the bounding temperatures, where the Carnot efficiency represents the maximal efficiency of a heat engine, by defining a relative efficiency.

$$\eta_{rel} = \frac{\eta_{abs}}{\eta_{carnot}} = \frac{\eta_{abs}}{\frac{\Delta T}{T_{hot}}} = \frac{T_{hot} \oint_{cycle} HdM(T, H)}{\Delta T * \rho \int_{T_{cold}} C_p(T) dT} \propto \frac{\Delta M}{\Delta T} \quad (1.5)$$

Therefore, the efficiency of the system is the amount of magnetic energy stored in the ferromagnetic material divided by the amount of thermal energy required to raise it by  $\Delta T$  (i.e.  $\Delta M/\Delta T$ ). Maximizing the device efficiency requires maximizing the magnetic energy in the ferromagnetic material while minimizing the amount of thermal energy input required to induce a phase transformation (i.e. minimize  $\Delta T$ ).

## 2.0 Harvesting About the Curie Point: Single Domains

After a considerable amount of research, UCLA believes the critical feature limiting the efficiency is the domain wall. The premise of this claim is that as the magnetic material is reduced beyond a critical volume that it becomes energetically favorable for every magnetic spin to be perfectly aligned, even after the initial biasing field is removed. This state is known as Single Domain (SD) and can be further characterized by a lack of domain walls and a remenant magnetization of greater than 90% of the materials saturation magnetization. We initially focused on Gd, due to its room temperature  $T_c$ , and evaluated the magnetic energy output change as a function of thermal input for different sizes with a focus on single domain limit.



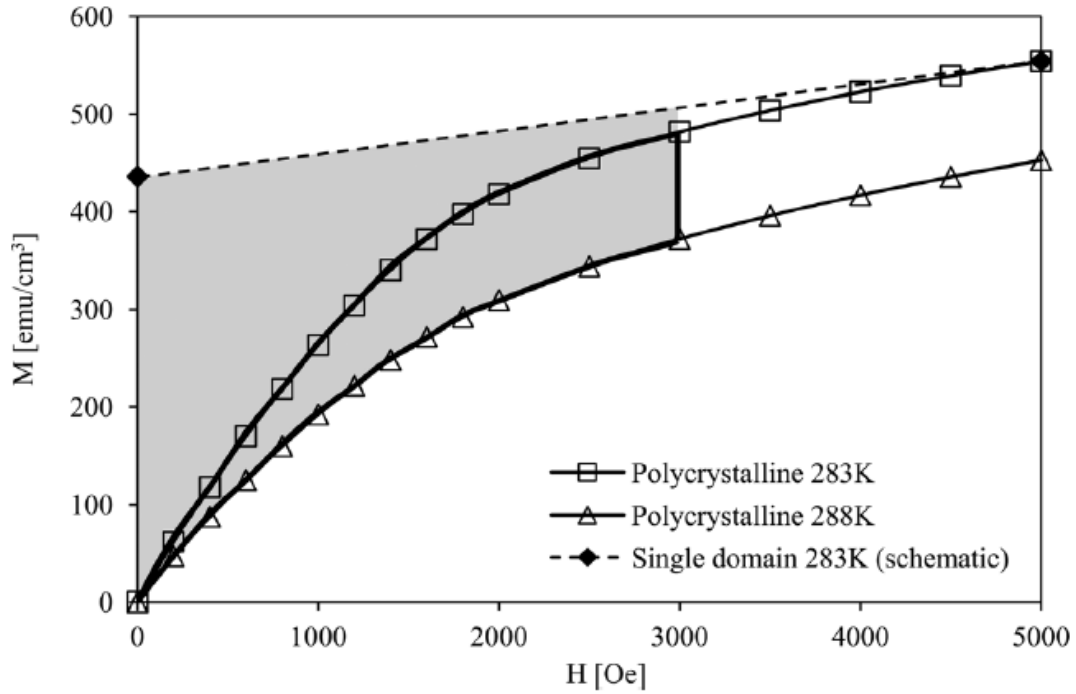
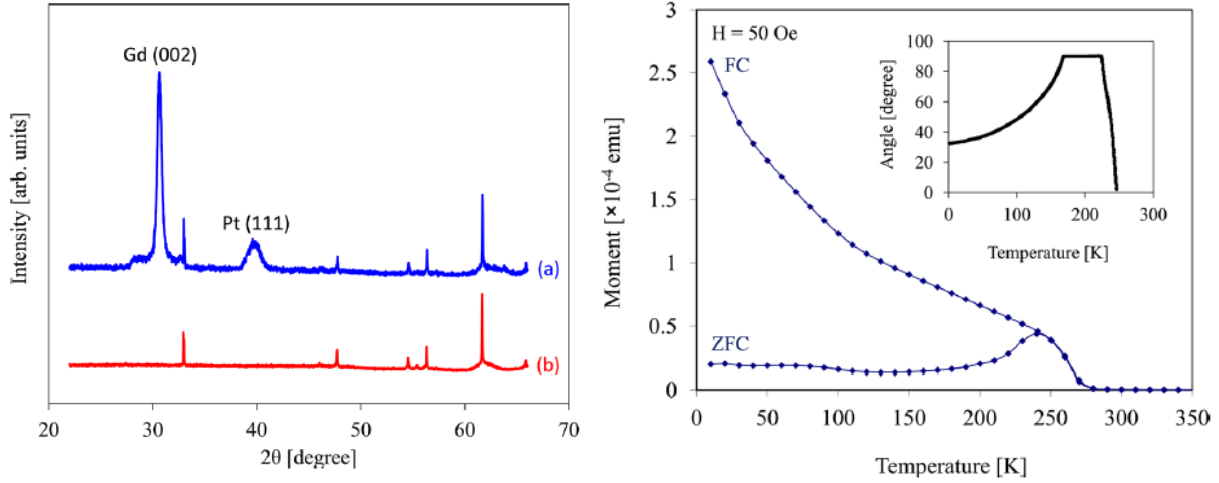


Figure 4: Isothermal magnetization curves of gadolinium at an applied field  $H_a=3000$  Oe

Figure 4, Hsu et al<sup>8</sup>, shows Isothermal magnetization curves for Gd in its polycrystalline film and SD forms. It can be seen that the area between curves represents the work produced during a single thermomagnetic cycle operating; in this case, the temperature difference between the curves was chosen to be  $\Delta T=5$  K. At a length scale below the SD limit, the remanent magnetization approaches the saturation magnetization at 3000 Oe, and the work potential of the system increases dramatically from  $24.2 \text{ kJ/m}^3$  to  $69.2 \text{ kJ/m}^3$ .

We began our experimental work by attempting to fabricate single domain elements of Gd, as this element could be characterized about both its  $T_c$  and SR regions. This was initiated by attempting to evaporate Gd using the CHA Industries Solution Evaporator available at UCLA's Integrated Systems Nanofabrication Cleanroom (ISNM). Even though these samples were capped with about 10 nm of self-passivating platinum (Pt), we were unable to achieve the magnetization values present in the literature. We determined that this was due to the fact that the cryopump used to maintain the vacuum was only rated for  $5 \times 10^{-7}$  Torr, which was insufficient to prevent oxidation from occurring in Gd during the evaporation process. As evaporation systems are also unable to produce crystalline films, we changed to an ultra high vacuum (UHV) sputtering system. The Denton UHV sputtering system was capable of achieving  $5 \times 10^{-8}$  Torr and was run in DC sputtering mode in an Argon (Ar) atmosphere with a pressure of

$10^{-3}$  Torr with a flow rate of 20 SCCM. The 99.9% pure Gd target was sputtered at 30 W and a deposition rate of  $\sim 1 \text{ \AA/s}$  to a thickness of 25 nm and was then capped with 20 nm of Pt before breaking vacuum.



**Figure 5: Left – XRD results for 20 nm sputtered Gd thin-film (a) and the Silicon substrate (b). Right – ZFC-FC results for a temperature range of 10 to 350 K.**

The sputtered film was examined by x-ray diffraction (XRD) to test for crystallinity and superconducting quantum interference device (SQUID) magnetometry to examine how the magnetization changed with temperature using the zero-field cooling/field cooling (ZFC-FC) technique. These results are presented in Figure 5. It can be seen from the XRD intensity plot that the Gd film showed a high degree of crystallinity with a sharp peak in the [002] direction, corresponding to the C-axis direction of the hexagonal crystal. The ZFC-FC measurement was taken in the in-plane orientation using a SQUID and showed a distinct hump between 220 and 260 K, indicating that the magnetic moment rotated into the direction of measurement. This anomaly is consistent with measurements for single crystal Gd<sup>9,10</sup> and shows that the film was deposited with sufficient epitaxy to achieve spin reorientation, which is an interesting distinction between this work and the previously published work by Berger et al.<sup>10</sup> wherein no temperature dependent magnetic rotation occurred. Their explanation was that sufficiently thin films exhibit such a large shape anisotropy that rotation into the out of plane direction should be entirely energetically unfavorable. We believe that grain boundaries observed in their film acted as effective defects which interfered with the long range order required to produce spin reorientation, but that the large degree of epitaxy observed in our films facilitated the spin reorientation response.

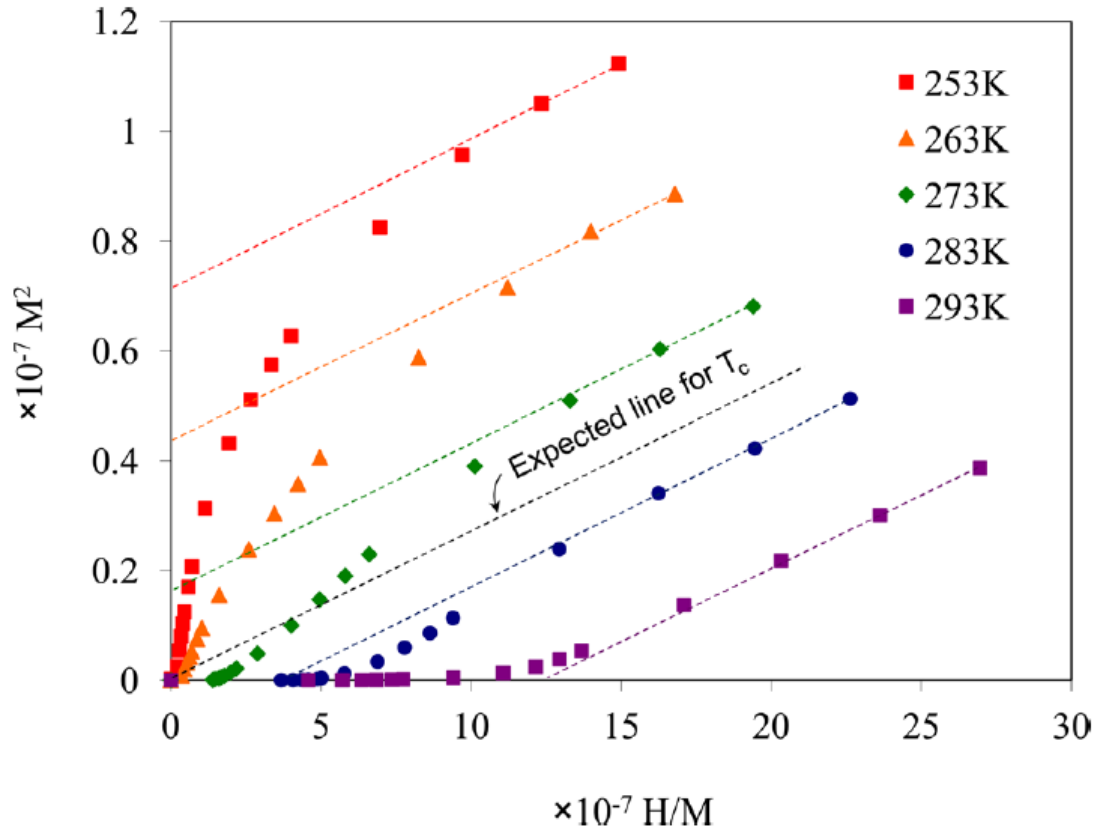
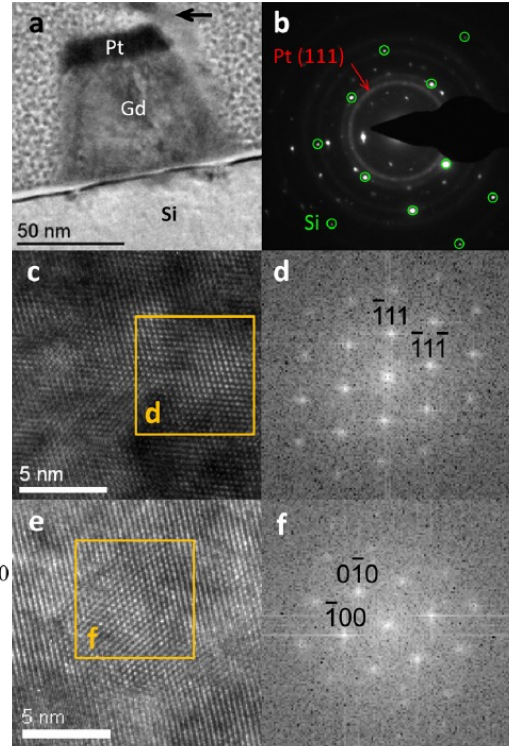
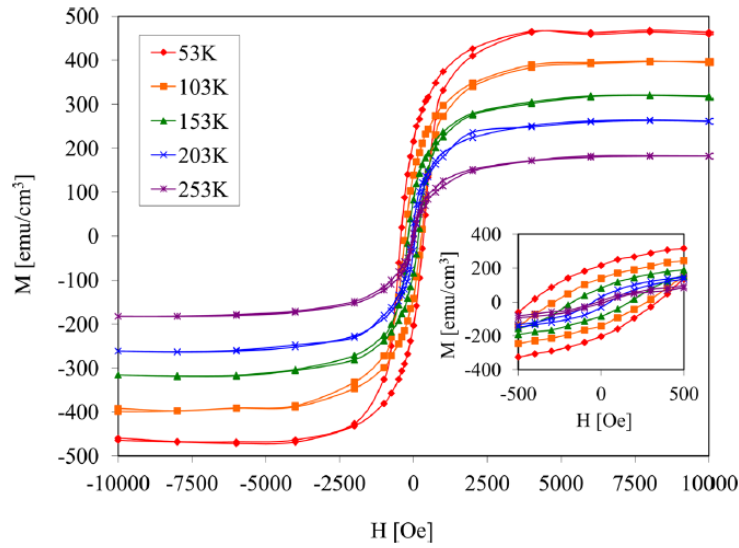


Figure 6: Arrott plot for 25 nm sputtered Gd thin film

Figure 6 presents the Arrott plot consisting of  $M^2$  vs  $H/H$  values obtained from the isothermal magnetization data of our epitaxial Gd thin films. The curves are generated from measurements conducted at five different temperatures. The Curie temperature is canonically defined from an Arrott plot as the temperature whose curve, when extrapolated, intersects the origin. For this Gd film, it was found that the saturation magnetizations measured at the lower temperatures are similar to those presented by Dan'Kov et al.<sup>12</sup>; however, the measured values became disparate at higher temperatures. The Arrott plot from our film shows that the Curie temperature of this film is approximately 278 K, representing a roughly 15 K shift from the bulk critical point at  $\sim 298$  K, which we verified from our evaporation source ingot. In the literature, shifts in the Curie temperature were also observed in various epitaxial<sup>12</sup> and sputtered<sup>13</sup> Gd films. We attribute the change of  $T_c$  in our sample to internal stresses which were introduced during the sputtering process. This process of shifting  $T_c$  is an interesting one because it shows that by modifying the crystal and magnetic ordering of a material, in this case by depositing a very thin film epitaxially, it is possible to tune the thermomagnetic behavior.



**Figure 7: Left - Isothermal magnetization curves of Gd nanobar array. Right – (a) TEM image of Gd nanobar, (b) Diffraction pattern of nanobar cross-section, (c) HRTEM of nanobar, (d) Select area FFT image with FCC zone, (e) HRTEM image of nanobar, (f) Selected area FFT image of HCP zone.**

When the same deposition process was used in combination with a lift-off procedure to produce nanostructures, in an attempt to create single domain elements, the saturation magnetization and coercivity results proved unsatisfactory. These results can be seen on the left side of Figure 7. From the M-H curves it was observed that the saturation at 53 K is less than  $500 \text{ emu/cm}^3$ , when it should be closer to  $2000 \text{ emu/cm}^3$ , and has a coercivity of less than 500 Oe. This most probably indicates a non-uniform crystallinity. It was also expected that, due to the magnetocrystalline anisotropy change across the spin reorientation transition, there would be a change from easy to hard axis as the temperature was increased, however that was not observed in the nanostructures. Given these disparities, we examined the nanobars under a high resolution transmission electron microscope (HRTEM), Figure 7 Right, where we noticed that the Pt capping layer failed to coat the sidewalls after lift-off, leading to a dramatic reduction in the amount of ferromagnetic material present by oxidation, and that different regions of the bars had different crystal structures; the cubic (FCC) zone seen in subset (d) produces significantly less magnetocrystalline anisotropy than the hexagonal (HCP) zone in subset (f).

The reduction in saturation magnetization along with the absence of shape anisotropy induced single domains in the Gd nanobars can be attributed to oxidation as well as non-uniform morphologies in the films crystallinity. The presented results show that the crystallographic ordering, and uniformity of the film has a substantial impact on the magnetic anisotropy and magnetic moment of Gd nanostructures.

We also investigated a wide range of single element materials where experimental data was readily available. Table 1 outlines some of the materials explored in their single and polycrystalline states, their Curie temperatures ( $T_c$ ), as well as the calculated relative efficiencies when operating about  $T_c$ .

**Table 1: Thermomagnetic Elements**

<u>Element</u>	<u>Poly/Single Crystal</u>	<u>T<sub>c</sub>(K)</u>	<u>Curie Point Operation <math>\eta_{Rel}</math></u>
Ho	Poly	20	50%
	Single		57%
Er	Single	20	29%
Dy	Poly	89	4%
	Single		23.32%
Tb	Poly	220	8.5%
	Single		12.5%
Gd	Poly	293	10.34%
	Single		20.5
Ni	Poly	531	2.5%
Fe	Poly	1044	9.5%
Co	Poly	1390	1%
Y <sub>2</sub> Fe <sub>17</sub>	Poly	Variable	9.87%

An operating temperature differential ( $\Delta T$ ) of 5K was considered about each materials  $T_c$  and was used to compute the relative efficiencies; the specifics of which can be found in Hsu et al<sup>8</sup>. From the table it can be observed that Holmium (Ho) and Erbium (Er) maintain the largest relative efficiencies when oscillating about their Curie Points. While different reasons have been postulated, UCLA believes it is the transition from a ferromagnetic to antiferromagnetic state, using an ordered to ordered transition, rather than a typical ferromagnetic to paramagnetic transition (i.e. order to disorder). The transition of

materials from ferromagnetic to paramagnetic results in significantly more entropic losses in the system, in turn causing a reduction of the energy that can be potentially harvested. UCLA began to explore other transition mechanisms (i.e. order to order) beyond those previously studied by the classical thermomagnetic community.

One such order-to-order transition is the Spin Reorientation (SR), a transformation which involves a thermally induced rotation of the magnetic easy axis from one crystalline direction to another. Horner and Varma<sup>14</sup> first visited the idea in 1968 and theorized that certain materials could make a spontaneous transition from an in-plane to an out of plane magnetization state due to the temperature dependence of magnetocrystalline anisotropy. Magnetocrystalline anisotropy is defined as the preferential alignment of a material's magnetic moment along a specific crystallographic axis, which arises from changes in the crystal-electric field as the lattice expands thermally.

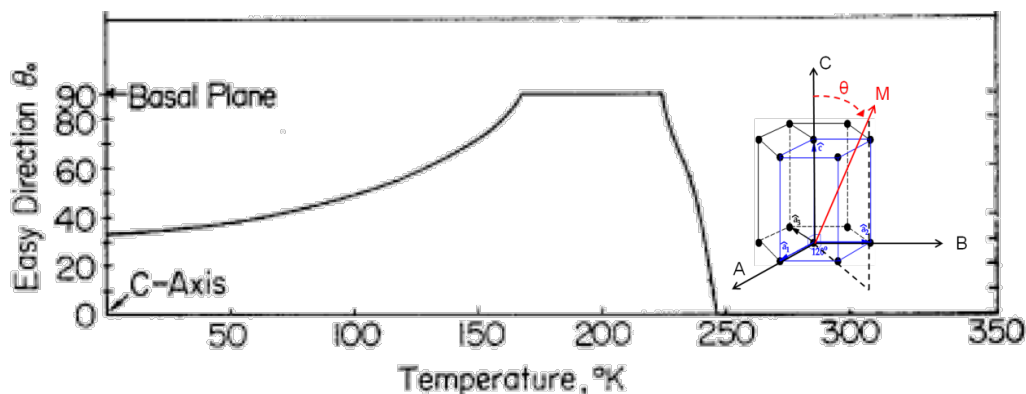


**Figure 8: Magnetic easy axis of gadolinium as a function of temperature**

Figure 8, a plot by Graham<sup>15</sup> augmented to provide a visualization of hexagonal crystal axes, shows Gadolinium's magnetization orientation (defined by theta ( $\theta$ ), the deviation from the C-axis) as a function of temperature for a single crystal. At deep cryogenic temperatures the magnetic easy axis is approximately at 33 degrees with respect to the C-axis, or approximately half way between the basal plane (B-plane) and the C-axis. As the temperature is increased to approximately 160 C, the B-plane becomes the preferred orientation. As the temperature changes from 230 K to 250K, a noticeable magnetic reorientation is observed; that is, the easy magnetization rotates 90° from the basal plane to the C-axis. This experimental data indicates that Gd has a Spin Reorientation Temperature ( $T_{SR}$ ) at 250° K. If one were to imagine that a single domain element of gadolinium were wrapped in a theoretical coil, then as the element was heated from 230 to 250K, the magnetization would rotate from the B axis to

the C axis and this flux change would generate current in the wire, i.e. electrical energy. Utilizing this foundation, we began exploring the integration the SR phenomenon into a harvesting methodology.

### 3.0 Spin Reorientation: Bulk Modeling

Our first task was to model the thermal to magnetic transduction mechanism, which was initiated by modeling a system at the bulk scale. We chose single crystal Gd as the working element and integrated its magnetocrystalline parameters, found experimentally by Graham<sup>15</sup>, into the COMSOL finite element package magnetics module. The ideal geometry for a flux yoke, given the orthogonal magnetization paths during a spin reorientation transition, was provided by Ohkoshi<sup>16</sup>.

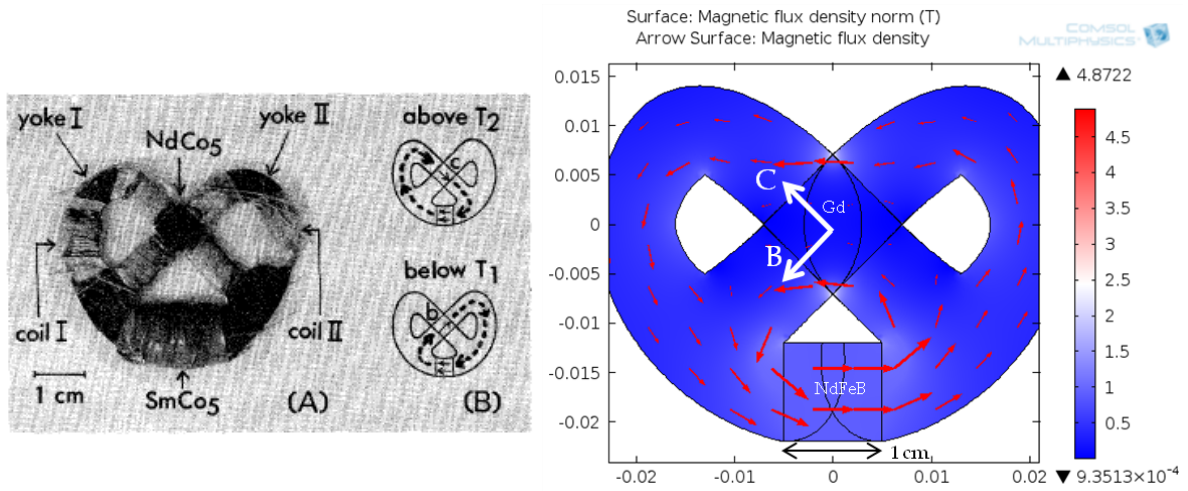


Figure 9: Left - The proposed magnetic flux return yoke by Ohkoshi; Right - The system modeled in COMSOL above  $T_{SR}$

Figure 9 Left, illustrates Ohkoshi's original design showing that below the SR temperature the magnetic flux would flow along the right loop of the "pretzel", corresponding to the B-plane direction of the NdCo<sub>5</sub> crystal, and would switch to the left path, corresponding to the C-axis, as the temperature was increased beyond the SR point. Coils 1 and 2, wrapped around the left and right paths respectively, would see an induced current as the spin reorientation occurred. In our model we replaced the NdCo<sub>5</sub> with Gd, due to our familiarity and the availability of material properties, and the SmCo<sub>5</sub> biasing magnet with NdFeB, a hard magnet which provides a larger magnetic field which was unavailable during Ohkoshi's study. In a system such as this, the amount of voltage induced within a theoretical coil, wrapped around each path, is monotonically related to the permeability change of the material which makes up the flux path by Lenz's Law.

$$V_{emf} = \frac{\frac{d\mu}{dt} * A \oint \frac{dH}{dt} dL}{L} \quad (3.1)$$

In this equation  $\mu$  is the permeability,  $t$  is time,  $A$  is the cross-sectional area of the flux path,  $H$  is the magnetic field and  $L$  is the length of the magnetic circuit. As the area, path length and applied field remain invariant, only the permeability's change contributes to the energy output. Magnetic steel was chosen as flux path material in this study due to its relatively high permeability under the applied bias field of 3 kOe, such that the spin reorientation in the Gd would induce the largest possible change in the yoke.

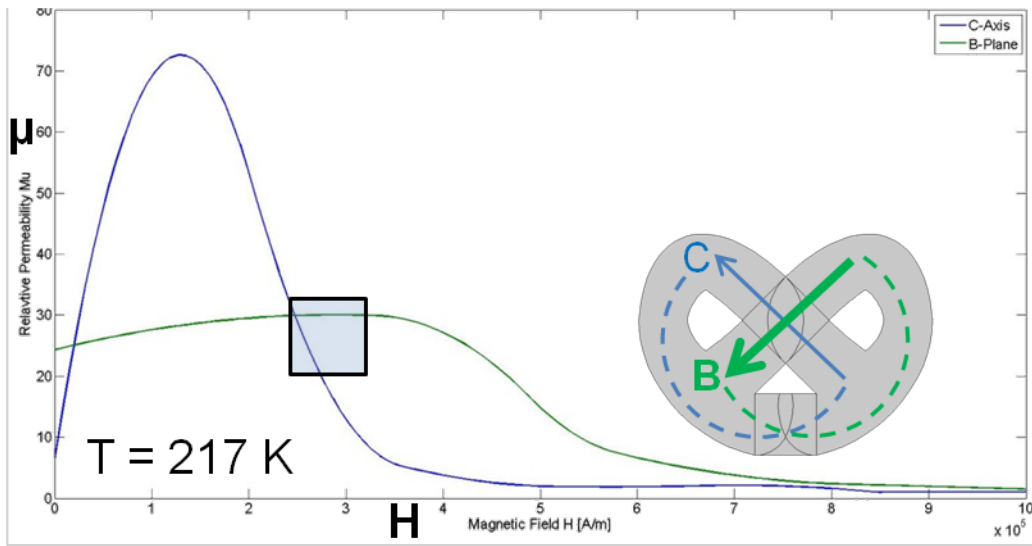


Figure 10: Permeability of the steel yoke as a function of applied field at 217K along both flux paths



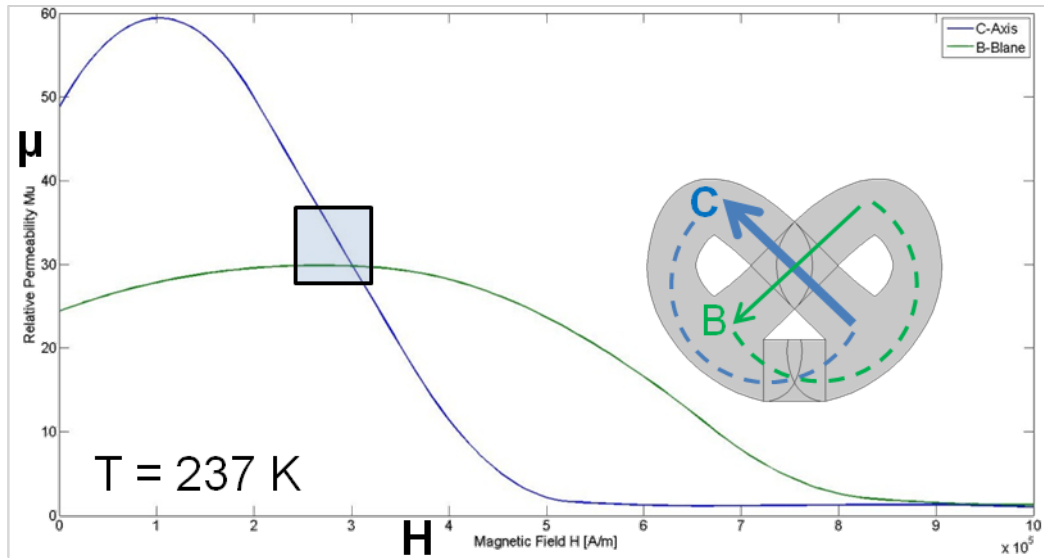


Figure 11: Permeability of the steel yoke as a function of applied field at 237K along both flux paths

The permeability of the yoke in each path direction was investigated for each temperature in the SR region. Figures 10 and 11 show the permeability of the yoke in the spin reorientation zone at 217 and 237K respectively. It should be recognized that in the field region required to saturate Gd in either direction, highlighted by the blue box, that the permeability of each flux path changes the most across the SR temperature differential, flipping from B-plane dominated to C-axis. This region was chosen as the operating zone for further study.

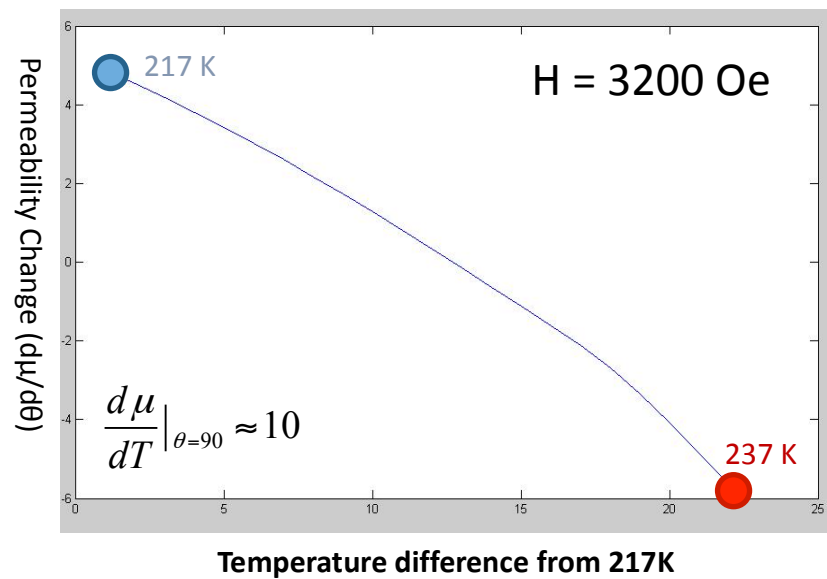


Figure 12: The permeability change of the yoke across gadolinium's SR region at an applied field of H=3200 Oe

Figure 12 shows the change in permeability as a function of temperature at the saturating field. From the figure it can be seen that as the magnetization of the gadolinium rotates 90°, that the relative permeability of the steel yoke changes by approximately 10. Using Lenz's law to back out an induced voltage yields an energy density of 5.1 kJ/m<sup>3</sup>. With this value being only a fifth of the energy predicted when operating about T<sub>c</sub>, we took a step back to analyze the thermodynamics of the spin reorientation transition.

#### 4.0 Thermodynamic Modeling of Spin Reorientation

In order to determine the ideal parameters for harvesting energy using a SR transition we required a better understanding of the thermodynamics that occur as magnets are thermally cycled. A model was developed to describe how each magnetic contribution to the total energy varied with temperature with considerations given to the different thermodynamic processes that occur across T<sub>c</sub> and SR. The following section outlines the formulation used to create this model.

In the most basic magnetic system, the magnetic contribution of the energy is  $E_o = \frac{\mu_o}{2} (H_T^2)$  where H<sub>T</sub> is the total field and μ<sub>o</sub> is the permeability. If one assumes that at an initial state there is no magnetic medium, then the total magnetic energy in a system results from an externally applied field (H<sub>A</sub>) only. If the system is modified to include a magnetic material and the applied field is considered to be external to the system, then the magnetic energy of the enclosed system can be represented as  $E = \frac{\mu_o}{2} (H_T^2 - H_A^2)$ . Here the difference between the squares of the field quantities represents the local energy encapsulated in a control surface surrounding the boundary of the magnetic media. That field quantity H<sub>T</sub> has contributions due to the applied external field and a demagnetization field (H<sub>D</sub>) which acts to oppose the external field within the magnetic material, resulting in the following.

$$E = \frac{\mu_o}{2} \left( (H_A - H_D)^2 - H_A^2 \right) = \frac{\mu_o}{2} \left( H_A^2 + H_D^2 - 2H_A H_D - H_A^2 \right) \quad (4.1)$$

After expanding and simplifying the result, the relation  $H_D = \left( \frac{B_D}{\mu_o} - M \right)$  is applied to obtain the

“demagnetization energy” in terms of the magnetization (M) of the magnetic material and flux due to the demagnetization field (B<sub>D</sub>). This formula is then expended as follows.

$$E = \frac{\mu_o}{2} \left( H_D \left( \frac{B_D}{\mu_o} - M \right) + 2H_A H_D \right) = \frac{\mu_o}{2} \left( \frac{H_D B_D}{\mu_o} - H_D M + 2H_A H_D \right) \quad (4.2)$$

The first term of the expanded Equation 4.2 can be represented as the following volume integral in all space:

$$\left( \frac{H_D B_D}{\mu_o} \right) = \frac{1}{\mu_o} \int_{A.S.} H_D g B_D dV \quad (4.3)$$

Where the demagnetization field  $H_D$  is equal to the negative gradient of a scalar field,  $-\nabla\phi$ , to yield Equation 4.5.

$$\frac{1}{\mu_o} \int_{A.S.} -\nabla\phi_D g B_D dV = \frac{-1}{\mu_o} \int_{A.S.} (\nabla g (\phi_D B_D) - \phi_D (\nabla g B_D)) dV \quad (4.4)$$

By using the electrostatic Maxwell relation, that the divergence of B is equal to zero, the second term can be reduced to zero. From there, the volume integral over all space can be converted into a surface integral, by Gauss' Law, to yield Equation 4.6.

$$\frac{-1}{\mu_o} \int_{A.S.} ((\phi_D B_D) g_n) dS \quad (4.5)$$

As the surface approaches infinity, such that  $\lim_{r \rightarrow \infty} (r^3 \phi) \rightarrow 0$  and  $\lim_{r \rightarrow \infty} \left( r \frac{d\phi}{dn} \right) \rightarrow 0$ , which implies that

$\phi_D \rightarrow 0$ , the entirety of Equation 4.3 can be seen to approach 0. Equation 4.2 can then be simplified to yield Equation 4.6.

$$E = \frac{\mu_o}{2} (-H_D M + 2H_A H_D) \quad (4.6)$$

The relation  $H_D = \left( \frac{B_D}{\mu_o} - M \right)$  is then applied to the second term, in order to have both energies in terms of magnetization. Simplifying the total energy transforms Equation 4.6 into the following.

$$E = -\frac{\mu_o H_D M}{2} + H_A B_D - \mu_o H_A M \quad (4.7)$$

Once again the product of a field and a flux, in this case  $H_A B_D$ , goes to zero by invoking electrostatic Maxwell relations and Gauss theorem. Then equating the demagnetization field ( $H_D$ ) to the product of a shape factor matrix ( $N$ ) and the magnetization such that  $H_D = -NM$ , provides a continuum energy function for a magnetic system as Equation 4.8.

$$E = \frac{\mu_o}{2} M (NM) - \mu_o H_A M \quad (4.8)$$

From the Hamiltonian describing the magnetic system we know that two additional energy terms should be added to describe the quantum effects acting on magnetic system; one to describe the exchange energy ( $E_{EX}$ ) and one to describe the magnetocrystalline anisotropy energy ( $E_{MCA}$ ) arising from spin-orbit interactions and the crystal-electric-field.

$$E = \frac{\mu_o}{2} M (NM) - \mu_o H_A M + E_{EX} + E_{MCA} \quad (4.9)$$

Under the assumption of a single domain magnetic element, we can consider any rotation of the spins to be coherent and thus any two states will have identical exchange energies and we will henceforth drop the term. The magnetocrystalline anisotropy energy can take multiple forms depending of the point group of the crystal being considered. In this study we evaluated Gd and NdCo<sub>5</sub>, both HCP crystals who have  $E_{MCA}$  of the form:

$$E_{MCA} = K_1 \sin^2(\theta) + K_2 \sin^4(\theta) + K_3 \sin^6(\theta) + K_4 \sin^6(\theta) \cos(6\phi) \quad (4.10)$$

Using our single domain assumption and applying Equation 4.10 for the magnetocrystalline anisotropy yields a total magnetic energy as follows.

$$E_m = \frac{\mu_o}{2} M (NM) - \mu_o H_A M + K_1 \sin^2(\theta) + K_2 \sin^4(\theta) + K_3 \sin^6(\theta) + K_4 \sin^6(\theta) \cos(6\phi) \quad (4.11)$$

From this equation it can be seen that the terms can be described with independent magnetization [ $M$ ] and temperature [ $T$ ] which indicates that the magnetic energy is a free energy of the Helmholtz variety:  $F = U - TS = E_M - SdT$ . One must then add to that the energy associated with the crystal lattice. Due to considering temperature as an independent variable, one must account for the effects of thermal energy on the lattice, via the temperature dependent heat capacity of the system.

$$dQ = C_p dT \rightarrow Q = \int_0^T C_p(T) dT \quad (4.12)$$

In the transition from an internal energy to a free energy this term takes on a negative sign from the standard Legendre transform yielding the Helmholtz free energy as Equation 4.12 subtracted from Equation 4.11. For ease of measurement we want a thermodynamic system in independent temperature [T] and magnetic field [H], the variables most easy to prescribe, we transform the system into a Gibbs free energy by the following:  $G = F + \mu_o H_A M$ . This yields a total Gibbs free energy as

$$G = \frac{\mu_o}{2} M (NM) + K_1 \sin^2(\theta) + K_2 \sin^4(\theta) + K_3 \sin^6(\theta) + K_4 \sin^6(\theta) \cos(6\phi) - \int_0^T C_p(T) dT \quad (4.13)$$

In order to quantify the work done per cycle, the total entropy of the system is defined as the negative partial derivative of the Gibbs free energy with respect to temperature,  $S = -\frac{\partial G[G, T]}{\partial T}$ .

$$S = - \left( \begin{aligned} &\left( \frac{\mu_o}{2} \frac{\partial M}{\partial T} gNM + \frac{\mu_o}{2} M gN \frac{\partial M}{\partial T} \right) + \left( \frac{\partial K_1}{\partial T} \sin^2(\theta) + 2K_1 \sin(\theta) \cos(\theta) \frac{\partial \theta}{\partial T} \right) \\ &+ \left( \frac{\partial K_2}{\partial T} \sin^4(\theta) + 4K_2 \sin^2(\theta) \cos(\theta) \frac{\partial \theta}{\partial T} \right) + \left( \frac{\partial K_3}{\partial T} \sin^4(\theta) + 6K_3 \sin^5(\theta) \cos(\theta) \frac{\partial \theta}{\partial T} \right) \\ &+ \left( \frac{\partial K_4}{\partial T} \sin^6(\theta) \cos(6\phi) + 6K_4 \sin^5(\theta) \cos(\theta) \cos(6\phi) \frac{\partial \theta}{\partial T} - 6K_4 \sin^6(\theta) \sin(6\phi) \frac{\partial \phi}{\partial T} \right) \\ &- C_p[T] \end{aligned} \right) \quad (4.14)$$

The total energy change is thus equivalent to the amount of heat that flows into the system:  $Q = \int S dT$ , where the magnetic change under the variation in temperature constitutes the work:  $W = \int S_{mag} dT$ . Note that the magnetic contribution of the entropy includes every term except for the lattice heat capacity  $C_p$ . The absolute efficiency of the system can then be denoted as the magnetic work over the total heat input.

$$\eta_{abs} = \frac{\Delta W}{\Delta Q} = \frac{\Delta S_{mag}}{\Delta S} \quad (4.15)$$

As thermodynamic cycles are subject to the Carnot limit, the ratio of the high temperature over the change in temperature, heat engines are typically compared by their efficiency relative to that limit by the following.

$$\eta_{rel} = \frac{\eta_{abs}}{\eta_{carnot}} = \frac{\Delta S_{mag} \Delta T}{\Delta S^* T_{hot}} \quad (4.16)$$

Using this standardized metric as well as the total magnetic energy density computed by Equation 4.15, Gd and NdCo<sub>5</sub>, operating in their spin reorientation regimes, were evaluated against one another as well as Gd operating about its Curie point.

## 5.0 Analytical Results

In order to compute the energy outputs and efficiencies of the relevant systems, Gd and NdCo<sub>5</sub>, the thermodynamic energy formulation was coded into Mathematica to facilitate a numerical solution for each process in the thermodynamic cycle. This was accomplished by first obtaining the saturation magnetization ( $M_s$ ), heat capacity ( $C_p$ ), and magnetocrystalline anisotropy coefficients ( $K$ 's) as functions of the temperature from the literature<sup>11,14-16</sup> and fitting each set with a spline, for continuous differentiability. Next we assumed that the shape of our magnetic elements were ellipsoidal, and thus applied Osborne shape factors<sup>14</sup> into the demagnetization tensor ( $N$ ). With values for every material and geometrical parameter coded in, we then went about computing the location of the magnetization as a function of temperature and applied field.

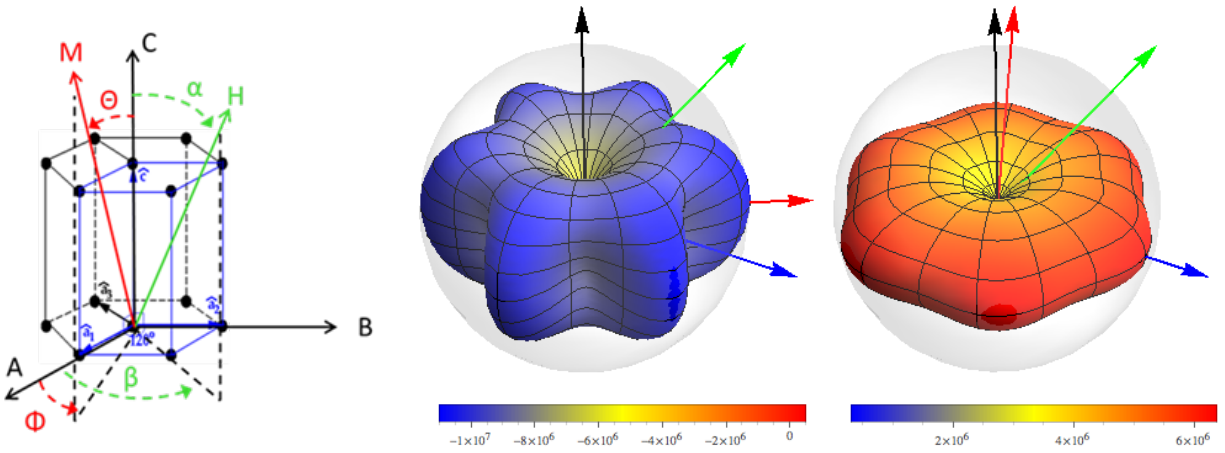
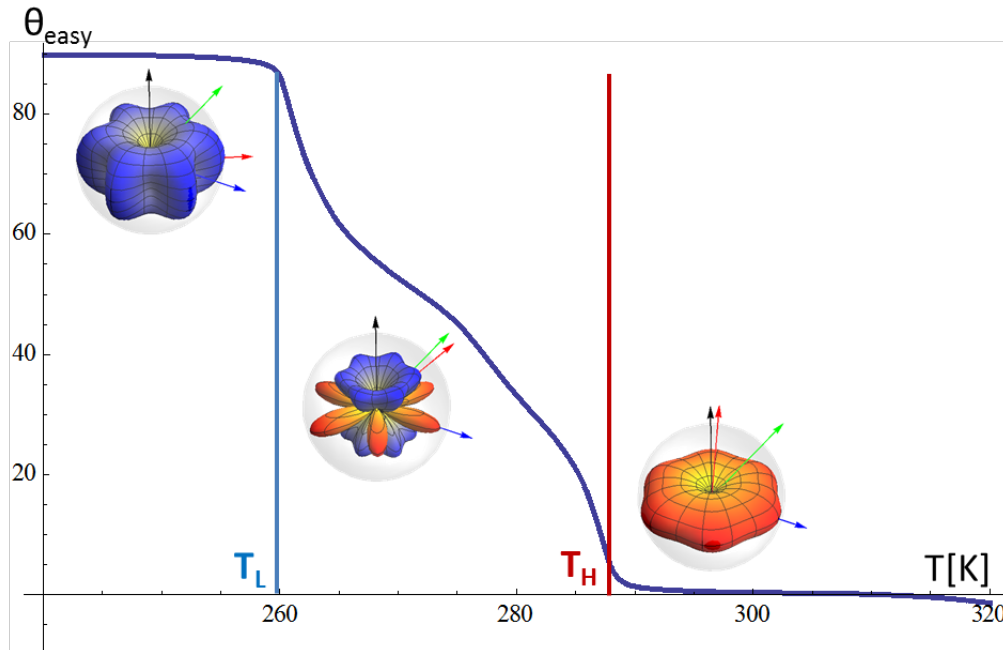


Figure 13: Left - Crystal orientation showing the applied field vector ( $H$ ) in green and its corresponding polar ( $\alpha$ ) and azimuthal ( $\beta$ ) angle as well as the red magnetization vector ( $M$ ) and its polar ( $\theta$ ) and azimuthal ( $\phi$ ) angles. In addition the black and blue arrows indicate the C and B axes respectively. Middle – The energy surface of a NdCo<sub>5</sub> sphere at  $T = 255K$  with a 100 Oe field applied at  $\alpha = 45^\circ$  and  $\beta = 45^\circ$ . Right – The energy surface of NdCo<sub>5</sub> at 286K with the same applied field parameters.

The numerical energy minimization used to determine the magnetization direction was computed from the total magnetic energy, Equation 1.12, by taking its partial derivative relative to the magnetization.

Due to the hexagonal crystal's six fold symmetry, this global minimization had the potential to return six magnetization vectors which were all equivalent in the absence of symmetry breaking applied field or shape effects. It was possible to obtain a set of quasi-static magnetization results which were discontinuous across a set of temperature values. Figure 13 provides two examples of the energy surfaces for NdCo<sub>5</sub>. It is apparent that NdCo<sub>5</sub> has an energy surface with 6 symmetrical energy wells, noting that blue surface corresponds to a negative total energy value and red to positive values; negative energy values are a result of the magnetocrystalline parameters, which are not normalized to 0 at absolute zero but rather at  $T_c$  when magnetic cohesion disappears. According to experimental studies<sup>15</sup>, the magnetization vector (shown in red) should move continuously from one set of angles to another. To remedy the potential discontinuities in the numerics, we broke the energy minimization into two parts.



**Figure 14: Magnetization angle for NdCo<sub>5</sub> through its spin-reorientation zone**

The first part was comprised of the global energy minimization, using Mathematica's built in "RandomSearch" method, to obtain a global minima at the starting temperature of interest. The second part started from the solution of the first and traversed the energy landscape to the nearest equivalent minima at the subsequent temperature values. This methodology guaranteed a continuous table of magnetization vectors, the axial angle is plotted in Figure 14 for NdCo<sub>5</sub>. Below the SR region, the 6 energy minima lay in the basal plane and as the temperature increases beyond 260K two easy cones

form, while energy maxima form along B-plane. As the temperature is increased beyond the SR region the energy minima collapses to the C-axis. In simple language, the easy axis rotates from 90 degree below 260 K to 0 degree above 286 K. With continuous functions of the magnetization direction computed, it was then possible to calculate the thermomagnetic work potential and efficiency of this transition.

**Table 2: Energy and Efficiency Results**

Material	Transition	$T_L$ [K]	$T_H$ [K]	$Q_{in}$ [J/m <sup>3</sup> ]	$W_{out}$ [J/m <sup>3</sup> ]	$\eta_{abs}$	$\eta_{rel}$
Gd	SR	219	243	4.67 E7	10.2 E5	0.02%	0.01%
Gd	Curie	283	288	1.31 E7	6.83 E5	0.52%	30.4%
NdCo <sub>5</sub>	SR	255	286	1.04 E8	2.57 E6	2.4%	22.2%

Using Equations 1.13 and 1.15 through 1.17 and the numerically computed magnetization states, the work and efficiencies were compiled into Table 2 for Gd spin reorientation, Gd Curie point operation, and NdCo spin reorientation. In these calculations the applied magnetic field was 100 Oe at  $\alpha$  and  $\beta$  equal to 45°, this guaranteed that the spin reorientations always occurred in similar directions. Additionally the operating temperature differential was chosen to increase the relative efficiency ( $\eta_{rel}$ ) for the given calculation rather than keep the temperature differential constant for each study. For Gd it can be seen that operating about its SR temperature actually provides a significant reduction in performance compared to its Curie point; compare 30% relative efficiency for Curie to 0.01% relative efficiency for spin reorientation. NdCo<sub>5</sub>, on the other hand, showed an order of magnitude increase in work density increase, as well as an increase in absolute efficiency as compared to either Gd example in the Table 2. The relative efficiency, however, was about 8% smaller than the ideal Gd Curie point transition; this appears reasonable as the operating temperature differential is approximately 6 times smaller for Gd (i.e. 5 K) about its  $T_c$  than NdCo<sub>5</sub> (i.e. 31 K) about its SR which significantly reduces the Carnot limit. We checked the validity of the calculations by determining which term dominated Equation 1.15 across the operating temperature differential and compared its magnitude change to the experimental results available in the literature.



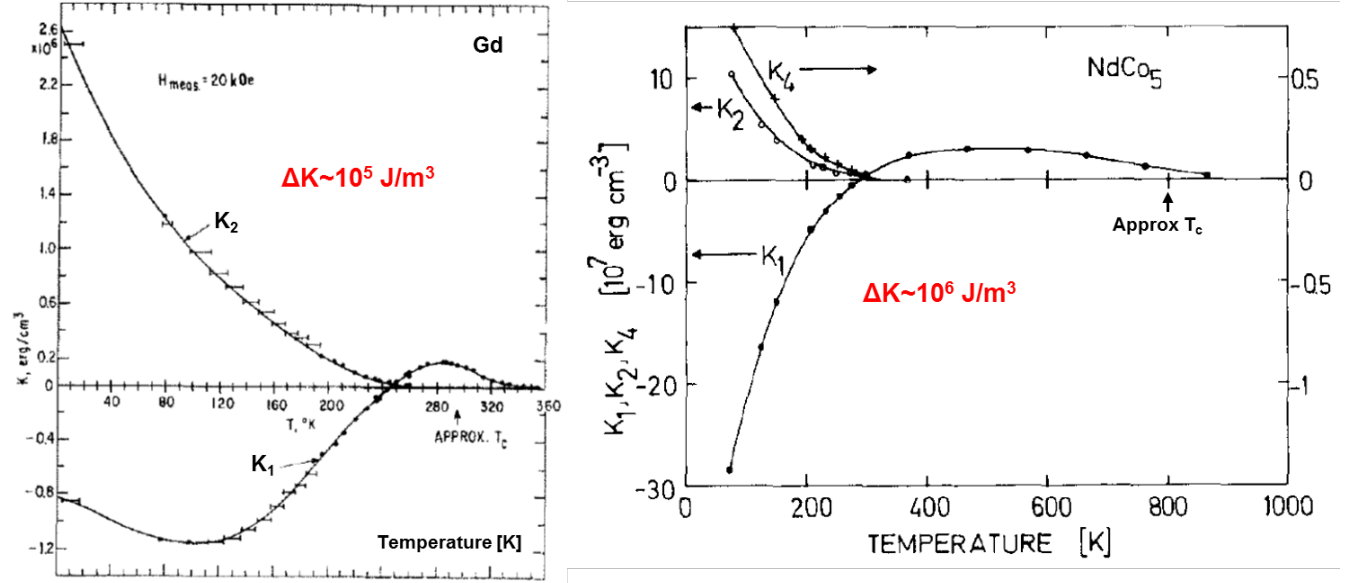


Figure 15: Left – Magnetocrystalline parameters of Gd from Graham<sup>10</sup>. Right – Magnetocrystalline parameters of NdCo<sub>5</sub> from Klein<sup>16</sup>. Each is demarked with the approximate energy change in the SR zone.

When the materials operate about their SR zones, the magnitude of their magnetization is nearly constant, and the majority of the temperature induced change takes place in the magnetocrystalline constants. Figure 9 provides the values for these parameters as functions of temperature. The temperature dependent magnetocrystalline change is approximately on the same order as the calculated work. For operation about the Curie point the magnetocrystalline terms reduce to nearly zero, such that only the magnitude of magnetization changes with temperature. The results for Gd about its Curie point, computing work from entropy, match the results in Hsu et al<sup>8</sup> where the work was computed from M-H loops.

A note should be made about the difference between the calculated results for NdCo<sub>5</sub> in comparison to results previously reporting a relative efficiency approaching 60%. In our original computation an error was made in determining the required heat input from the specific heat ( $C_p$ ). This term was reported by Ohkoshi<sup>16</sup> in units erg/(mol K) which was inappropriately converted to erg/(g K), instead of erg/(cm<sup>3</sup> K), due to lack of information regarding the density of NdCo<sub>5</sub>. A density of 8.35 g/cm<sup>3</sup> was determined by computing a hexagonal unit cell from the bond lengths and atomic sizes that were provided. This value is within 10% of computing the density by a rule of mixtures between the two elements and is thus considered relatively accurate. We postulated that even with the reduction in relative efficiency, that the order of magnitude increase in work and absolute efficiency warranted attempting to fabricate nano-scale elements to experimentally verify our calculations. The amount of energy being produced

and the “decent” relative efficiency of NdCo<sub>5</sub> still makes it an attractive candidate for thermal energy harvesting based on this work.

## 6.0 Spin Reorientation Experimental Effort

The following paragraphs focus on sputter deposition of thin film epitaxial NdCo<sub>5</sub>. While this was attempted we did not achieve our stated objective of creating an epitaxial thin film of NdCo<sub>5</sub>. Unlike elemental gadolinium, NdCo<sub>5</sub> is a bimetallic compound which requires precise stoichiometric control to achieve the desired magnetic properties. In the literature epitaxial thin films have been produced by pulsed laser deposition (PLD) using co-deposited single element targets<sup>18</sup>, however this method is currently unavailable to UCLA and in the potential event of desired scale-up would prove to be cost and time prohibitive. Thus we attempted to epitaxially deposit this material by co-sputtering.

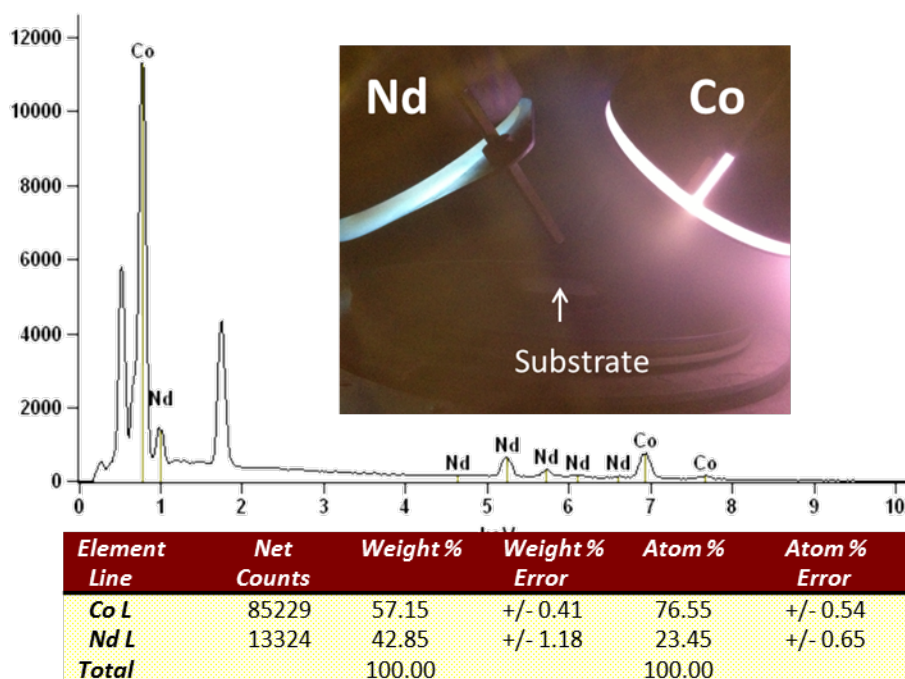


Figure 16: EDS results of Nd-Co deposition on Si substrate. Inset shows co-sputtering configuration.

Neodymium and cobalt targets of 99.9% purity were obtained from the Kurt J. Lesker Company and calibrated into our Denton UHV sputtering system. Figure 12 shows the co-sputtering configuration and our initial attempt to deposit the material on a silicon substrate. The parameters of deposition were an Ar pressure and flow rate of 2.5 mTorr at 20 SCCM, sputtering powers of 280 and 42 Watts for Nd and Co respectively, a pre-sputter time of 360 sec, and a target to substrate distance of 5cm. After depositing the 100 nm film, the composition was examined using electron diffraction spectroscopy (EDS)

to provide the atomic percentage of each element present. Stoichiometric  $\text{NdCo}_5$  should be 16.67% Nd and 83.33% Co, but our initial attempt showed approximately 5% more Nd content than desired.

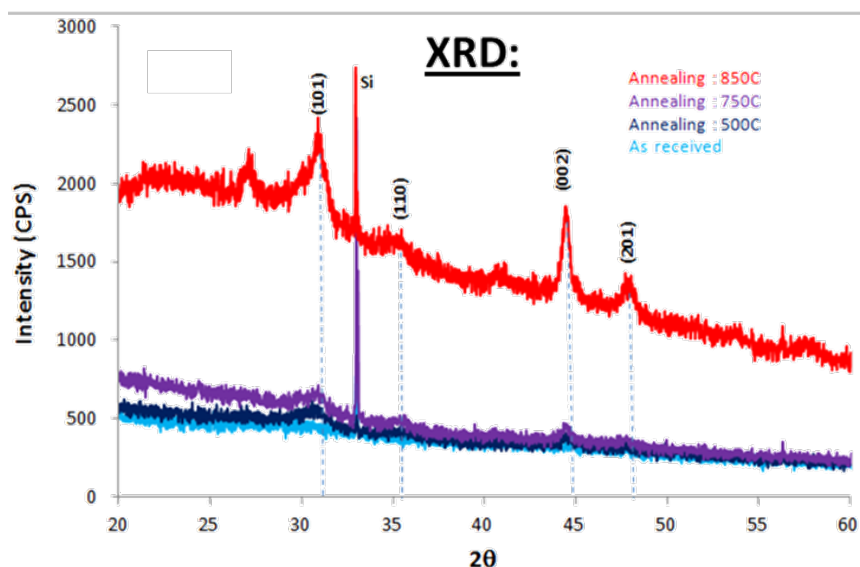


Figure 17: XRD results of recrystallization study on original Nd-Co deposition

Even with this disparity we performed measurements to create a baseline for recrystallization temperatures. This work included measuring the XRD response following annealing the sample in atmosphere at temperatures ranging between 500 and 850 C. The results are presented in Figure 13. The data shows that the sample became crystalline once annealed above 750 C. While a moderate peak presented itself along the (002) C-axis direction, the largest peak was in a cubic (101) direction. This can be partially attributed to compositional variation, but we suspected that the cubic Si substrate provided the greatest contributing factor and one that would not produce epitaxial  $\text{NdCo}_5$  structures. However, these results indicate that temperatures above 750 C are required to crystallize the deposited films.

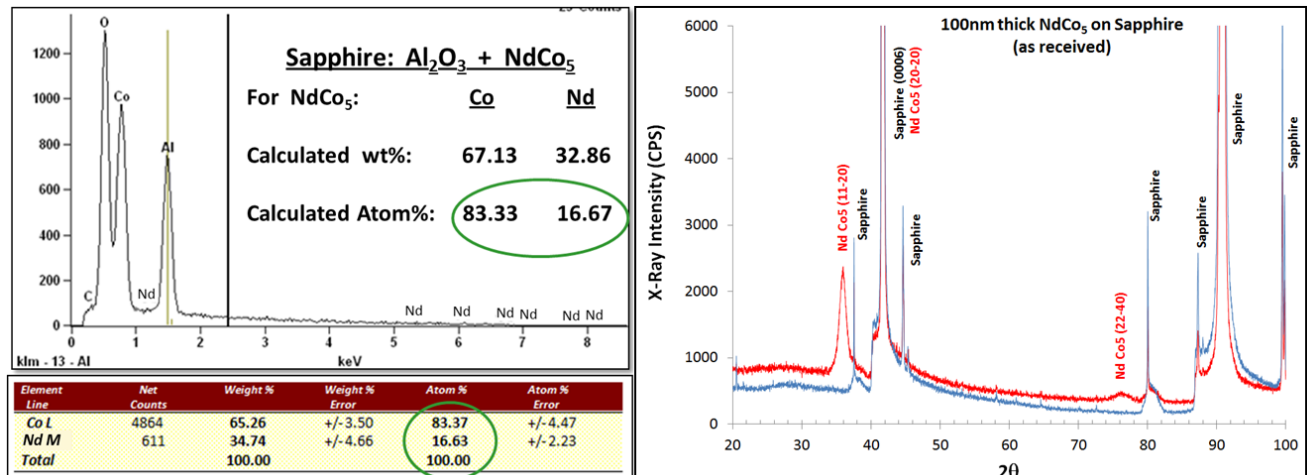
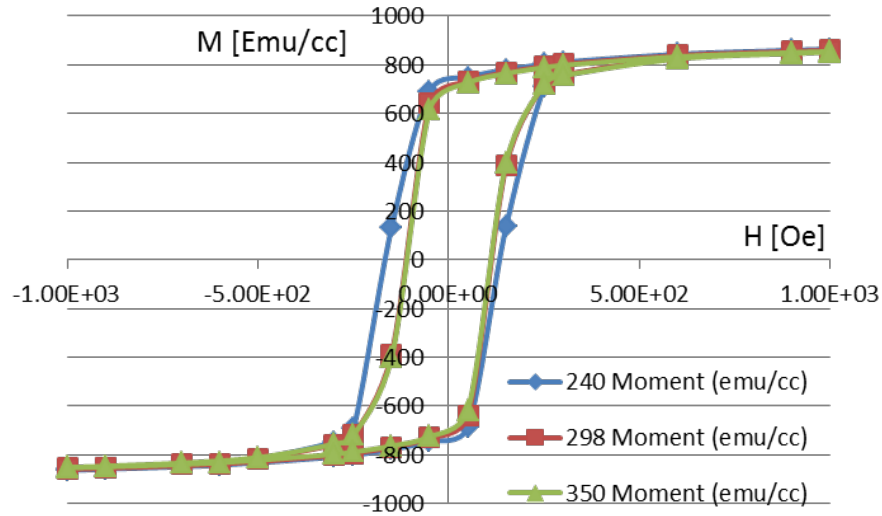


Figure 18: Left – EDS of 100 nm of  $\text{NdCo}_5$  film on sapphire. Right – XRD of 100 nm  $\text{NdCo}_5$  film on sapphire.

In subsequent runs we used a sapphire substrate, a hexagonal crystal with lattice parameters within 4% of the desired  $\text{NdCo}_5$  crystallography, to deposit the  $\text{NdCo}_5$  film. This substrate should produce an epitaxial film if the deposition rate and crystallization rate is adequately be controlled. During deposition on this substrate we conducted a parametric study proportionally modifying the driving power to the plasma sources to tune the  $\text{NdCo}$  composition. Figure 14 provides the EDS and XRD results for a  $\text{NdCo}_5$  sample once the appropriate deposition parameters were. From the EDS results, large peaks appeared corresponding to the aluminum and oxygen present in the substrate, however it can be seen that after subtracting out the counts due to the substrate that the desired  $\text{NdCo}_5$  composition was obtained (i.e. see circled composition in Figure 14). The XRD study in Figure 14 right was conducted on a both bare sapphire wafer and the unannealed film sample which showed very strong agreement between the lattice structures of the two materials, indicating that film was apparently epitaxial deposited without post deposition annealing. This result suggested that the deposition energy was sufficient to at least partially crystallize the film as a crystalline structure is observed in the XRD.



**Figure 19: Magnetization curves of 100 nm of NdCo<sub>5</sub> on sapphire**

Using the unannealed sample that appeared to be epitaxial deposited shown in Figure 14, the NdCo<sub>5</sub> film magnetic response was measured using SQUID at temperatures below (240) and above (298 and 350) the SR zone. The results are presented in Figure 15. The magnetization curves were taken in the out-of-plane (C-axis) direction. It was expected that the M-H loops would show a hard axis at less than 250 K, which would then transition to an easier axis, with a larger coercivity, above 280 K. Here it is important to also point out that the overall coercivity was only 200 Oe, much lower than the expected 2500 Oe at 350 K in a single crystal. We originally attributed the smaller coercive field to the lack of a fully crystalline material; we hypothesized that the materials contained both amorphous and crystalline regions through the thickness of the film producing a softer magnetic structure. To resolve the amorphous/crystalline problem we annealed a portion of the sample at 850 C. However, upon magnetic measuring of the annealed sample and subsequent measurements on composition, we found that the Nd content of the annealed portion dropped substantially. The remaining thin film contained only trace Nd content. At this stage we determined that, like Gd, a capping layer would be necessary to prevent loss of Nd.

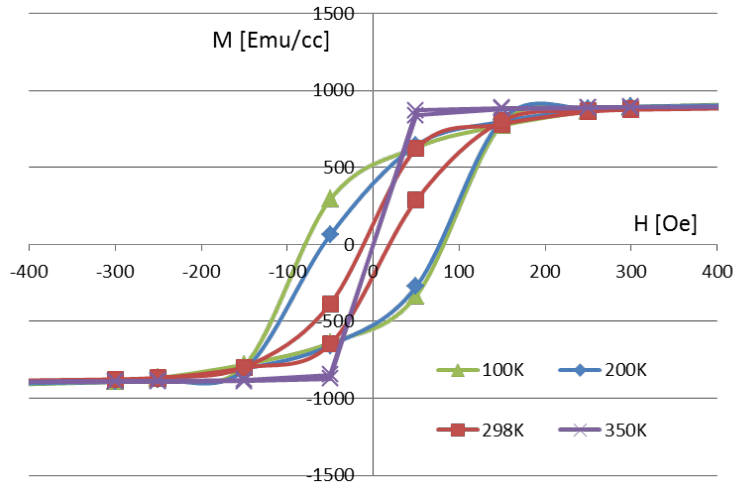


Figure 20: Magnetization curves for 100 nm of NdCo<sub>5</sub> on sapphire with 10 nm Ti capping layer

During the next set of depositions 10 nm of Ti was sputtered over the top of the NdCo<sub>5</sub> in-situ, before breaking vacuum. Ti was chosen because this target was in the shared resource facility already present in the sputtering system. The argon flow rate was reduced from 20 SCCM to 12 SCCM in an attempt to slow the deposition rate and attain a higher ordering of the NdCo<sub>5</sub> crystals. Figure 16 shows the magnetization curves for the Ti capped sample. Using the same experimental procedure in the SQUID with additional measurements performed at colder temperatures, a spin reorientation appears to be present between 200 and 350 K. While this temperature differential is much larger than expected, it showed that this deposition method had promise to achieve the desired effect. Additionally, we hypothesized that the lower coercivity value, 100 Oe compared to the predicted 2500 Oe, was due to internal stresses and could be rectified by annealing the sample to relax the crystal lattice.

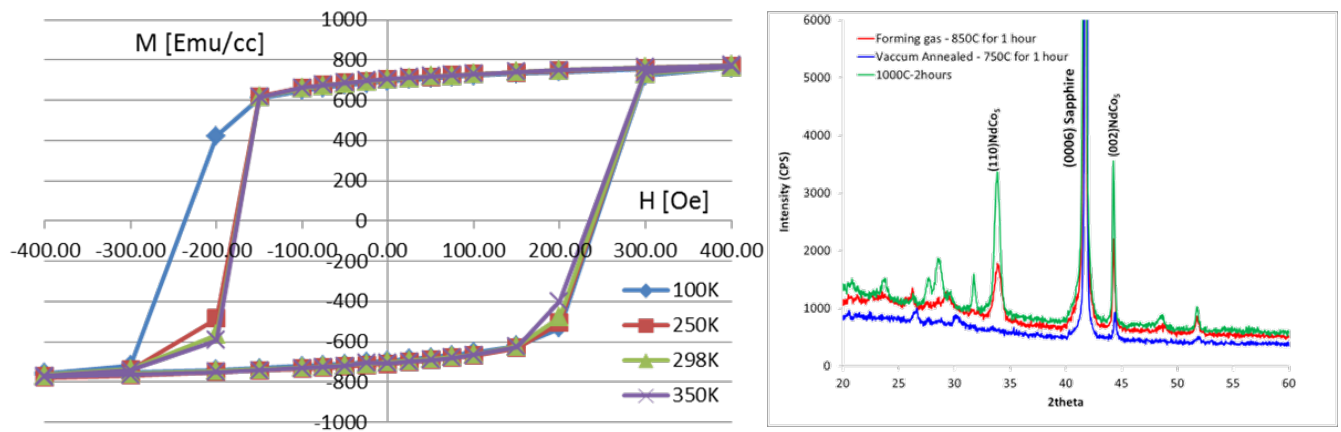
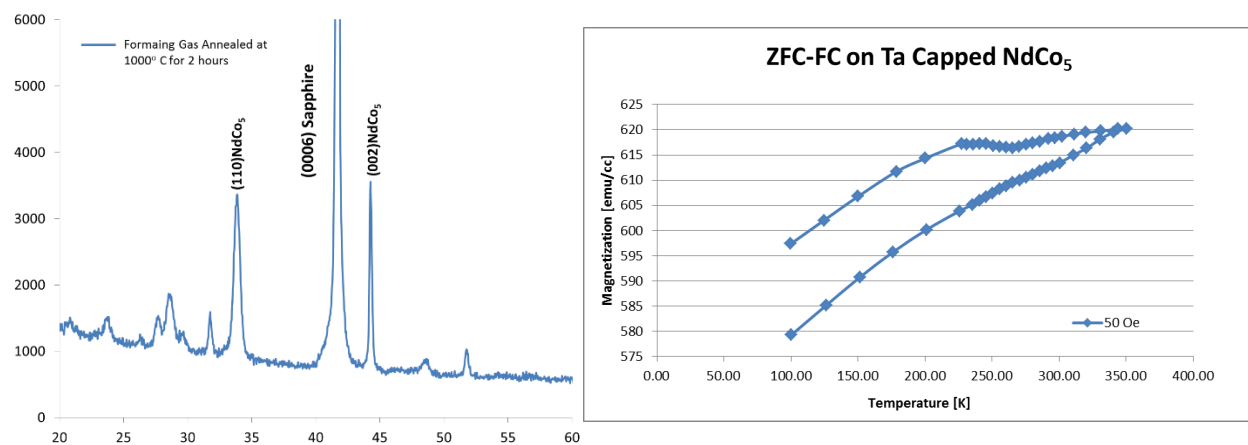


Figure 21: Left - Magnetization curves for 100 nm NdCo<sub>5</sub> on sapphire with 10 nm Ti and annealed to 850 C

This sample was subsequently annealed to 850 C, for 1 hour, in a tube furnace under a reducing environment, 90% argon/10% hydrogen to prevent oxidation. Figure 17 shows the results of the repeated magnetization curves after annealing and subsequent XRD. It can be seen that the annealing increased the coercivity from approximately 80 to nearly 250 Oe, which was attributed to a reduction in film stress and potential relaxation of the crystals into a more ordered state. Unfortunately, the reorientation observed before annealing was absent. The XRD appears to indicate that post annealing relaxes a portion of deposited film into a cubic form, with a notable peak forming in the (110) direction as well as the hexagonal (002). Additionally, WDS results showed that the Ti capping layer was depleting the Nd during the annealing process. To prevent this reaction in subsequent depositions, future runs were capped with tantalum (Ta), a material which is much more stable and less reactive at high temperatures.



**Figure 22: Left – XRD results for Ta capped NdCo<sub>5</sub> after 2 hour anneal at 1000° C for 2 hours; Right – ZFC-FC results for the same sample between 100 and 350 K.**

Figure 18 shows the crystallography and temperature dependent magnetization results for one of the stoichiometric NdCo<sub>5</sub> samples capped in Ta after a 2 hour anneal at 1000° C. The XRD plot shows peak counts very similar to the Ti coated sample in Figure 17, indicating that the sample crystallized during the annealing process. A WDS stoichiometry study (not shown) indicated NdCo<sub>5</sub> composition had been achieved. That is the values are close to those shown in Figure 14 left, both before and after annealing. Given the compositional and crystallographic success on this sample, we examined the samples magnetization as a function of temperature using ZFC-FC and found a valley at 250 K during the field cooling portion of the experiment. This anomaly in the in-plane magnetization measurements suggests that the magnetization is rotating into the direction of measurement at this temperature, matching the theoretical prediction. However, the magnitude of this change was only approximately 5 emu/cc, at an

applied field of 50 Oe. We postulated that the magnitude was smaller than anticipated due to the fact that this film appeared to be polycrystalline rather than textured. The less than fully crystallized regions contributed less to magnetization rotation due to being less thermomagnetically coupled. Magnetization loops at constant temperatures were performed to confirm the hypothesized lack of global easy axis rotation.

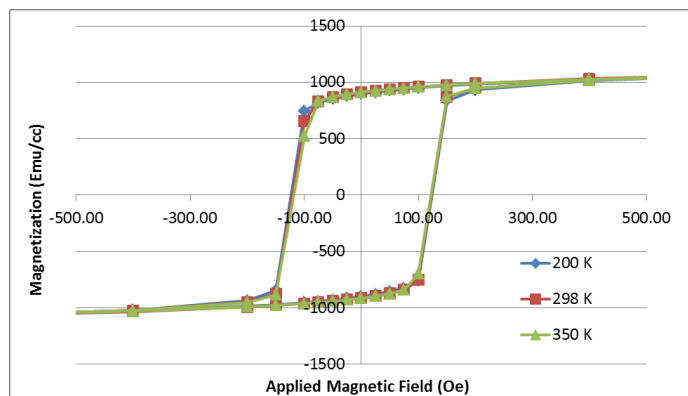


**Figure 23: Magnetization curves for Ta capped NdCo<sub>5</sub> annealed at 1000° C for 2 hours.**

The results in Figure 19 confirmed our suspicions that while the sample was noticeably crystallized, that the uniformity of the crystallization was not epitaxial. This can be observed in the small coercivity values, approximately 100 Oe instead of the expected 2500 Oe, and absence of a hard-axis curve for the measurements at 298 and 350 K. It was hypothesized that in order to achieve the required crystal epitaxy through the thickness of the film, to obtain spin reorientation, it would be necessary to heat the substrate at or above 850 during the co-sputtering processes; an ability that UCLA does not currently have. We attempted to reach out to colleagues at Stanford and Northeastern and are still in the process of doing this. More recently we have attempted field alignment, an application of 3000 Oe along the C-axis, during two different annealing processes: vacuum annealing at 750 C for 2 hours, the max that our cryo-pump could handle, and tube furnace annealing at 1000 C for 1 hour under the reducing environment. Neither of these methods significantly improved the crystal uniformity (i.e. epitaxy) or magnetic properties. The bottom line is that we believe that sputter deposition can be used to successfully deposit epitaxial, thin film NdCo<sub>5</sub>. However, in-situ substrate heating at 850° C is required with both minimal Ar pressure and under UHV. The substrate heating provides sufficient mobility of the co-sputtered material to nucleate textured crystal growth, deposit uniformly without large stresses, and remain contaminant and oxide free. While this was not successfully achieved during this program, we



are continuing this study in the next couple of months with vacuum annealing to be performed at Brookhaven National lab.

## Conclusion

Thermomagnetics, and specifically spin reorientation, show promising advantages over other thermal harvesting methods, namely an order of magnitude increase in work output and absolute efficiency. The thermodynamic model developed under this program represents an advancement for the community in studying this fairly unexplored area. The model predicts the theoretical work output from entropy and provides an analytical approach to compare different 2nd order thermomagnetic transformations. Future improvements to the model could include discontinuous 1st order systems. While the results computed for NdCo<sub>5</sub> are promising, when compared to Gd, they still fall short of the 50% relative efficiency mark we had originally hoped to obtain. They do, however, confirm one of our hypotheses that thermomagnetic transduction mechanisms of the order-to-order type have the potential to achieve a higher absolute efficiency. This is important because this work shows that the field of thermomagnetics is promising but the appropriate material has not yet been found that produces a relative efficiency sufficiently larger than currently exists. Finally, UHV Sputtering shows potential as a means of depositing crystalline thermomagnetic nano-structures, however additional work needs to be conducted to perfect the consistency with which these structures are produced.

## Works Cited

1. TESLA, N. Pyromagneto-electric generator. *US Pat. 428,057* (1890).
2. Brillouin, L. & Iskenderian, H. P. Thermomagnetic generator. *Electr. Commun.* **25**, (1948).
3. Elliott, J. Thermomagnetic generator. *J. Appl. Phys.* **300**, 1774–1777 (1959).
4. Kirol, L. & Mills, J. Numerical analysis of thermomagnetic generators. *J. Appl. Phys.* **83415**, 824–828 (1984).
5. Solomon, D. Improving the performance of a thermomagnetic generator by cycling the magnetic field. *J. Appl. Phys.* **60645**, 915–921 (1988).
6. Solomon, D. Thermomagnetic mechanical heat engines. *J. Appl. Phys.* **65**, (1989).
7. Solomon, D. Design of a thermomagnetic generator. *Energy Convers. Manag.* **31**, 157–173 (1991).
8. Hsu, C.-J., Sandoval, S. M., Wetzlar, K. P. & Carman, G. P. Thermomagnetic conversion efficiencies for ferromagnetic materials. *J. Appl. Phys.* **110**, 123923 (2011).
9. A. Berger, A. W. Pang, and H. Hopster, *Phys. Rev. B* **52**(2), 1078 (1995).
10. A. Berger, A. W. Pang, and H. Hopster, *J. Magn. Mater.* **137**(1–2), L1 (1994).
11. Dan’Kov, S. & Tishin, A. Magnetic phase transitions and the magnetothermal properties of gadolinium. *Phys. Rev. B* **57**, 3478–3490 (1998).

12. U. Stetter, M. Farle, K. Baberschke, and W. G. Clark, *Phys. Rev. B* **45**(1), 503 (1992).
13. O. Nakamura, K. Baba, H. Ishii, and T. Takeda, *J. Appl. Phys.* **64**(7), 3614 (1988).
14. Horner, H. & Varma, C. Nature of spin-reorientation transitions. *Phys. Rev. Lett.* **20**, 845–846 (1968).
15. Graham, C. Some Magnetic Properties of Gd Single Crystals. *J. Appl. Phys.* **34**, 1341–1342 (1963).
16. Ohkoshi, M., et al. Spin reorientation in NdCo single crystals. *AIP Conf. ...* 616–617 (1976).

# AFOSR Deliverables Submission Survey

Response ID:4589 Data

1.

## 1. Report Type

Final Report

## Primary Contact E-mail

Contact email if there is a problem with the report.

carman@seas.ucla.edu

## Primary Contact Phone Number

Contact phone number if there is a problem with the report

310-825-6030

## Organization / Institution name

MAE DEPT/UCLA

## Grant/Contract Title

The full title of the funded effort.

A Nano-Scale Based Thermal-Magnetic Energy Harvesting

## Grant/Contract Number

AFOSR assigned control number. It must begin with "FA9550" or "F49620" or "FA2386".

FA9550-09-1-0620

## Principal Investigator Name

The full name of the principal investigator on the grant or contract.

GREG CARMAN

## Program Manager

The AFOSR Program Manager currently assigned to the award

LES BYUNG-LIP LEE

## Reporting Period Start Date

09/01/2009

## Reporting Period End Date

01/31/2015

## Abstract

In this study we investigated/developed innovative thermomagnetic harvesting methods and materials that transduce waste heat into electrical energy. Initially we focused on gadolinium (Gd) single domain nanostructures which we predicted to have a thermomagnetic harvesting efficiency of approximately 30% of the Carnot limit. In this study, we discovered that more ordered transitions led to higher transduction efficiencies. Utilizing this phenomenon, we explored the effect of order-to-order spin reorientation harvesting in neodymium cobalt (NdCo5). Analytical modeling showed that NdCo5 could achieve an energy density greater than 2 MJ/m<sup>3</sup> with an efficiency of approximately 22% of the Carnot limit. This report overviews the body of literature related to the thermomagnetic field, provides a detailed analysis of the UCLA modeling effort, and describes fabrication and testing techniques used to create and evaluate nano-structured thermomagnetic materials. This work should encourage others in the community to begin a closer evaluation of thermomagnetic energy harvesting methods.

## Distribution Statement

This is block 12 on the SF298 form.

Distribution A - Approved for Public Release

## Explanation for Distribution Statement

If this is not approved for public release, please provide a short explanation. E.g., contains proprietary information.

## SF298 Form

Please attach your [SF298](#) form. A blank SF298 can be found [here](#). Please do not password protect or secure the PDF. The maximum file size for an SF298 is 50MB.

[carman-SF-298.pdf](#)

**Upload the Report Document. File must be a PDF. Please do not password protect or secure the PDF. The maximum file size for the Report Document is 50MB.**

[AFOSR Final Report CARMAN.pdf](#)

**Upload a Report Document, if any. The maximum file size for the Report Document is 50MB.**

## Archival Publications (published) during reporting period:

1. Hsu, C-J., Prikhodko, S.V., Wang, C.Y., Chen, L-J., and Carman, G.P., "Magnetic anisotropy in nanostructured gadolinium", Journal of Applied Physics, 111(5):053916 - 053921 (03/01/2012) DOI: <http://dx.doi.org/10.1063/1.3691220>
- 2 Hsu, C.J., Sandoval, S.M., Wetzlar, K.P. and Carman, G.P., "Thermomagnetic conversion efficiencies for ferromagnetic materials", Journal of Applied Physics, 110(12):123923 - 123930 (12/15/2011)
3. Hsu, C-J., Hockel1, J.L., and Carman, G.P., "Magnetoelectric manipulation of domain wall configuration in thin film Ni/[Pb(Mn1/3Nb2/3)O3]0.68-[PbTiO3]0.32 (001) heterostructure", Applied Physics Letters, 100(9):092902 - 092905 (02/27/2012) DOI: <http://dx.doi.org/10.1063/1.3690953>
4. Wetzlar K. and Carman G.P. "Analytical Modeling of Thermomagnetic Spin Reorientation," to be submitted.

## Changes in research objectives (if any):

NONE

## Change in AFOSR Program Manager, if any:

NONE

## Extensions granted or milestones slipped, if any:

## AFOSR LRIR Number

## LRIR Title

## Reporting Period

## Laboratory Task Manager

## Program Officer

## Research Objectives

## Technical Summary

## Funding Summary by Cost Category (by FY, \$K)

	Starting FY	FY+1	FY+2
Salary			
Equipment/Facilities			
Supplies			
Total			

## Report Document

## Report Document - Text Analysis

## Report Document - Text Analysis

## Appendix Documents

## 2. Thank You

### E-mail user

May 20, 2015 15:33:03 Success: Email Sent to: carman@seas.ucla.edu